Iranian Journal of Catalysis 12(3), 2022, 283-293

IRANIAN JOURNAL OF CATALYSIS

Synthesis of Fe-doped TiO_2 with improved photocatalytic properties under Vis-L irradiation

Imane Ellouzi[a*], Boutaina Regraguy[a], Souad El Hajjaji[a], Mourad Harir[b,c], Philippe Schmitt-Kopplin[b,c], Hinda Lachheb[d] and Larbi Laânab[e]

a) Laboratory of Spectroscopy, Molecular Modeling, Materials, Nanomaterials, Water and Environment, CERNE2D, Faculty of Sciences, Mohammed V University, in Rabat Av. Ibn Batouta, BP 1014 Rabat, Morocco
b) Research Unit Analytical BioGeoChemistry, Helmholtz Munich, Ingolstaedter Landstrasse 1, 85764 Neuherberg, Germany
c) Chair Analyt Food Chem, Technical University Munich, Maximus von Imhof Forum 2, 85354 Freising, Germany
d) Unité de Recherche Catalyse et Matériaux pour l'Environnement et les procédés (URCMEP), Faculté des sciences de GABES/Université de Gabes. Campus Universitaire.Cité Erriadh 6072 Gabes, Tunisia
e) Laboratory of Conception and Systems, Faculty of Sciences, Av. Ibn Batouta, BP 1014 Rabat, Morocco

Received 4 October 2021; received in revised form 23 June 2022; accepted 3 July 2022 (**DOI: 10.30495/ijc.2022.1941684.1875**)

ABSTRACT

Fe-doped TiO_2 nanoparticles were successfully synthesized by the coprecipitation method. TiO_2 was doped with a different molar ratio of iron amounts, namely 0.1% and 0.2%. An undoped TiO_2 was also prepared for comparison. X-ray diffraction (XRD), transmission electron microscopy (TEM) and UV-visible diffuse reflectance spectroscopy techniques were used to characterize the as-synthesized nanoparticles. The XRD spectra revealed that the photocatalysts were mostly in a well-crystallized anatase phase. Optical properties of the powders shifted from UV to the beginning of the visible light (Vis-L) region. Absorption edge wavelengths between 392 and 380 nm were obtained for the Fe-doped TiO_2 and TiO_2-P25, corresponding to band gap energies between 3.17 and 3.26 eV. TEM images showed homogeneity with a certain degree of agglomeration for all the samples. The photocatalytic efficiency of the as-synthesized Fe-doped TiO_2 nanoparticles was performed using azo dye methyl orange (MO) in an aqueous solution under Vis-L irradiation. The photocatalytic results showed that Fe-doped TiO_2 nanoparticles effectively degrade MO under Vis-L excitation and follow pseudo-first order kinetics. Besides, kinetic comparison showed that pure TiO_2 is less efficient than 0.1% and 0.2% Fe-doped TiO_2 because they exhibit unequaled efficiency. Moreover, the photocatalyst at 0.2% Fe-doped TiO_2 molar ratio revealed the highest photocatalytic efficiency, which was 4.2 times higher compared to pure TiO_2. Different amounts of Fe induced different increases in the apparent first-order rate constant of the photocatalytic process.

***Keywords**: Titanium dioxide; Coprecipitation; Photocatalytic degradation; Iron; MO.*

1. Introduction

Development of chemical wastewater treatment has improved the oxidative degradation of organic compounds. Among the new oxidation processes, the heterogeneous photocatalysis of advanced oxidation processes (AOP) which is considered as an emerging destructive technology leads to the mineralization of organic pollutants [1]. It is the use of semiconductors as an effective and promising method to eliminate organic pollutants from the environment [2, 3]. For instance, semiconductor metal oxide photocatalysts have been widely studied in various green applications, especially wastewater purification [4, 5]. Among the studied semiconductors, titanium dioxide (TiO_2) has attracted much attention due to its long-term stability, low cost, non-toxicity, and strong photocatalytic activity [6]. It has three different crystal forms (i.e., anatase, rutile, and brookite). The band gap energies of anatase and rutile TiO_2 are 3.23 and 3.02 eV, respectively. Although anatase TiO_2 has high photocatalytic activity, anatase has a flaw in relation to its low specific surface area, low thermal stability, low mechanical potency and lack of wear strength [7-9]. The large band gap of TiO_2 (3.2 eV)

---

[*] Corresponding author:
E-mail address: *im.ellouzi@gmail.com*,
(**I. Ellouzi**)

severely limits its practical application [10, 11]. The use of Vis-L is rather weak, the rapid recombination of electron-hole pairs, and the difficult-to-separate solution properties lead to major limitations in the light efficiency of using TiO_2. While the photoactivity of supported TiO_2 is low due to the interaction of TiO_2 with the support during heat treatment, pure TiO_2 limits its application in photochemistry [12].

To overcome this problem, several approaches have been used (i.e. metallic or non-metallic iron doping) [13]. Further studies have been conducted to reduce the band gap of anatase to absorb Vis-L by doping it with transition metal ions [14]. In fact, Fe^{3+} ions have attracted much attention in Ti^{4+} due to their half-filled d-electron structure and the same ionic radius, which means that Fe^{3+} ions can be integrated into the TiO_2 lattice structure [15, 16]. In addition, the doping of Fe^{3+} ions reduces the recombination of photo-generated electrons and holes, thereby enhancing the photocatalytic activity of TiO_2 [17]. Nowadays, different synthesis ways have focused on improving the doping of materials (i.e., iron, nitrogen, and selenium) to enhance the photocatalytic efficiency [18-23]. Several methods have been proposed to synthesize TiO_2 nanoparticles including co-precipitation [24], sol-gel methods [25], spray pyrolysis [26] and chemical vapor deposition [27]. Dyes used in the textile industry are major pollutants, however, they could be decomposed by TiO_2 nanoparticles [28-30]. About half of the world's production of synthetic textile dyes (700,000 tons per year) belongs to azo products, which have chromophore (–N=N–) moieties [31]. Fifteen percent of total world production of dyes is lost during the dyeing process and is released in textile effluents [32, 33].

Overall, industrial effluents not only produce a strain on water bodies, but also cause environmental damage to living organisms by stopping the re-oxygenation process of water and stopping sunlight diffusion, which disrupts the natural growth activity of aquatic life. Moreover, some dyes pass into drinking water and can harm human life, as some dyes are noxious with potential carcinogenic properties. It is therefore essential to remove dyes from water bodies or treat them in a way that minimizes environmental damage and discolors the water [37-39]. There is currently a wide range of wastewater treatment technologies (i.e., precipitation, ion exchange, solvent extraction, filtration and electrochemical treatment) [40-42]. However, all of these methods have significant disadvantages mainly related to incomplete ion removal, high-energy requirements, and production of toxic sludge or other wastes that require subsequent disposal. Thus, the efficiency and simplicity of advanced oxidation processes (AOPs) have made them a suitable choice for the removal of toxic chemicals from wastewater in recent years [43-47].

MO is one of the azo dyes, among its various types. The chemicals associated with azo dyes are azo stains, insoluble in water and other liquids [34, 35]. Effluents from dyeing plants are strongly colored and toxic. Ninety percent of reactive textile dyes enter the activated slurry treatment plants, flow into rivers and cause serious problems such as (a) decrease in penetration of sunlight in the streams, (b) poisonous for fish and mammal life, (c) stops the growth of microorganisms, and (d) some positively charged compounds (like triphenylmethanes) affect the plants and animals [36]. Thus, Fe-doped TiO_2 photocatalysts have been studied for the degradation of MO as a model azo dye under Vis-L irradiation. The objectives of this study are: (i) to prepare, (ii) to characterize, and (iii) to test the effects of Fe dopants on the structural and optical properties of TiO_2 P25 nanoparticles synthesized by the co-precipitation method, in parallel with their photocatalytic performances.

2. Experimental

2.1. Catalyst synthesis

All chemicals were used without further purification. Degussa P25 titanium dioxide was used as the photocatalyst. It is mostly in the anatase 80% and rutile form 20% and has a BET surface area of 50 m^2/g with a mean particle size of 20 nm. TiO_2 semiconductor nanoparticles were prepared by the coprecipitation method to obtain Fe-doped TiO_2 powders with different percentages (0.1 or 0.2 wt %). $FeCl_3$ or $FeSO_4$ used as precursors for iron dopant were added to 1.5g of TiO_2 ($Fe/TiO_{2\,=}$ 0.1 or 0.2 wt %) were dissolved in 30 ml of HCl (0.25 M) solution and was dispersed under ultrasonic vibration for 2h to ensure the homogeneity.
The solution was stirred and NaOH (0.1M) was added into the solution as a coprecipitant agent to adjust the pH value. During this process, the solution became milky white, and the white precipitates were slowly formed. After that, the mixture was washed. The solution was filtered and the precipitate was dried in an oven at 50 °C. The dried powders were ground with a mortar and then calcined at 500 °C for 2h.

2.2. Structural characterization techniques

The phase composition of the samples was determined by X-Ray Diffraction, it was used to identify crystallinity of the studied samples. Patterns of samples were obtained using a Bruker AXS D-8 diffractometer using Cu-Kα radiation in Bragg-Brentano geometry in the 2θ range from 20° to 80°. The optical properties of TiO_2 were recorded on a UV-1600 spectrophotometer. The structural morphology of the prepared powders was revealed by transmission electron microscopy (TEM) using the Tecnai G2 microscope at 120 kV microscope.

2.3. Photocatalytic activity measurement

The photocatalytic performance of TiO_2 was evaluated using MO as the representative organic pollutant. Photocatalytic dye decolorization experiments were performed in a rectangular glass reactor filled with cold water. Photocatalytic degradation experiments were carried out in a 125 mL quartz tube, which was installed inside the reactor. The irradiation of a 200 W hydrogen lamp was used as a Vis-L resource. The prepared TiO_2 nanoparticles (0.5 g/L) were suspended in 125 ml of Methyl Orange (10 ppm) solution. The suspension was stirred in the dark for 45 min to make sure that the mixture had achieved adsorption/desorption equilibrium; 2 ml of the solution was taken out at regular time intervals. Then the light was switched on, the powder was filtered through 0.2 μm pore size microporous membranes to separate the photocatalyst's particles. The concentration of the degraded solution was recorded by UV-Vis Spectrophotometer at 464 nm.

3. Results and Discussion

3.1. XRD

The crystalline phase was identified by X-ray diffraction. The peaks at 25.3^0 (101), 37.69^0 (004), 48.07^0 (200), 54.28^0 (211), 55.21° (105) and 65.79^0 (204) are plainly representative of the tetragonal anatase TiO_2 structure (**Fig. 1**). The highest peak intensity was detected in the (101) direction at 2θ=25.3°. All of these XRD diffraction patterns conform to JCPDS card No. 21-1272. These diffraction peaks are thoroughly combined with anatase TiO_2 structure. No rutile or brookite diffraction peaks were detected in the doped TiO_2 powders. Similar patterns were observed for all photocatalysts with different mole percentages of iron. Moreover, no other crystalline phases (i.e., Fe_2O_3 or Fe_xTiO_y) were found, which could be attributed to the raised metallic dispersion [48] or the low-concentration Fe doping process. Regardless of the amount of Fe dopant, all Fe-doped TiO_2 photocatalysts consist solely of iron oxide-free TiO_2 anatase structure. The absence of iron oxide indicates that Fe^{3+} ions are successfully incorporated into the TiO_2 anatase framework without the formation of iron oxide on the TiO_2 surface. Increasing the amount of iron reduces the intensity of the peaks (**Fig. 1**). The maximum peak of the (101) plane is slightly shifted, predicting that iron ions are incorporated into the TiO_2 network and displace Ti^{4+} by being located at interstitial sites, or they are dispersed on the surface [49-50]. The average crystallite sizes were determined using the Scherrer formula as shown in Eq (1):

$$D = 0.94\,(\alpha/\beta)\cos\theta \qquad \text{Eq (1)}$$

Where D is the crystallite diameter, λ is the wavelength of the X-ray radiation (C_uK_α=1.5406 Å), shape factor k is related to the crystallite shape, usually taken as 0.9. The average crystallite size is determined using Eq (1) and the values are summarized in **Table 1**. We observed that the amount of Fe has no significant effect on the sizes and distributions of the photocatalysts and increases with the addition of dopants.

3.2. TEM

Transmission electron microscopy (TEM) is used to study the morphology of the synthesized Fe-doped TiO_2 nanoparticles. **Fig. 2** shows the TEM image of Fe = 0.2% doped TiO_2. The surface of the doped nanomaterial has a morphology similar to that of the undoped photocatalyst. Moreover, the shape of the doped TiO_2 nanoparticles is spherical and uniform. **Fig. 2** shows the size distribution histogram varying from 20 to 50 nm. Overall, TEM images evince the uniformity and a certain level of agglomeration of all samples.

3.3. DRS

Absorption spectra and DRS-UV visible spectra of TiO_2 and Fe-doped TiO_2 photocatalysts with different molar percentages of iron are shown in **Fig 3**. The optical properties of the prepared samples were examined using UV-vis diffuse reflectance in the wavelength range 300-800 nm. A reduction in TiO_2 powder transmittance is observed, reflecting the primary light absorption. All spectra have an abrupt absorption edge. The optical band gap (Eg) values of TiO_2 are determined from their absorption spectra. Eg values for band gap materials are calculated by plotting $(\alpha h\upsilon)^{1/2}$ as a function of (hυ), and extrapolating the linear portion of the curve until they intersect the photon energy axis (**Fig. 3**). To study the electronic band structure, the conduction and valence band edge positions of TiO_2 and Fe-doped TiO_2, conduction band (CB) and valence band (VB) were calculated using Eqs (2, 3) [50-52]:

$$E_{VB} = \chi - E_e + 0.5Eg \qquad \text{Eq (2)}$$

$$E_{CB} = E_{VB} - Eg \qquad \text{Eq (3)}$$

Where, χ is the absolute electronegativity of the semiconductor, E_{CB} and E_{VB} stand for conduction band (CB) and valence band (VB) potentials, respectively. The Eg and E_e represent the band gap energy of TiO_2 and the energy of the free electrons at the hydrogen scale (~4.5 eV), respectively. The calculated values are summarized in **Table 2**. As shown in **Fig. 4**, the potential position values obtained for CB and VB bands were used to draw a schematic energy diagram to illustrate the charge carrier transfer in the coupled system, which is presented in the following section.

The red shift is a frequently observed fact in transition metal-doped II-IV semiconductors, which is due to the insertion of Fe^{3+} cations into the lattice structure of TiO_2 resulting in oxygen vacancies [54]. Consistent with previous studies [54], **Fig. 4** confirms that Fe^{3+} cations generate an impurity band near VB due to oxygen vacancies, thereby effectively reducing the optical band gap. Comparison of UV-Vis spectra of undoped and doped TiO_2 show slight red shift from 3.26 eV to 3.17 eV at maximum absorption due to iron doping (**Table 2**). We can conclude that Fe^{3+} doping of TiO_2 semiconductors leads to a decrease in the value of Eg, which determines the activity of the resulting material under Vis-L. In particular, we observed that the higher the Fe content in the catalyst, the more pronounced the effect.

As expected, TiO_2 shows characteristic spectra with rising sharp edges of fundamental absorption at 385 nm. In the case of doped TiO_2, the absorption shifts to the visible range due to the presence of iron. The band gap energies are given in **Table 2**. The spectra of Fe-doped TiO_2 photocatalysts are identical to the absorption thresholds reported elsewhere using a similar approach and different dopants [55-56]. The basic elements of the photocatalytic decomposition of organic pollutants are, for instance, the valence band (VB) and conduction band (CB) of the photocatalyst. Meanwhile, the band gap energies of Fe-TiO_2 and TiO_2 are 3.17 and 3.26 eV, respectively (**Fig. 4**). According to the Eqs (2) and (3), the E_{VB} and E_{CB} values of Fe-TiO_2 were calculated to be 2.389 eV and -0.78 eV, respectively, while the E_{VB} and E_{CB} values of TiO_2 were 2.434 and -0.826 eV, respectively.

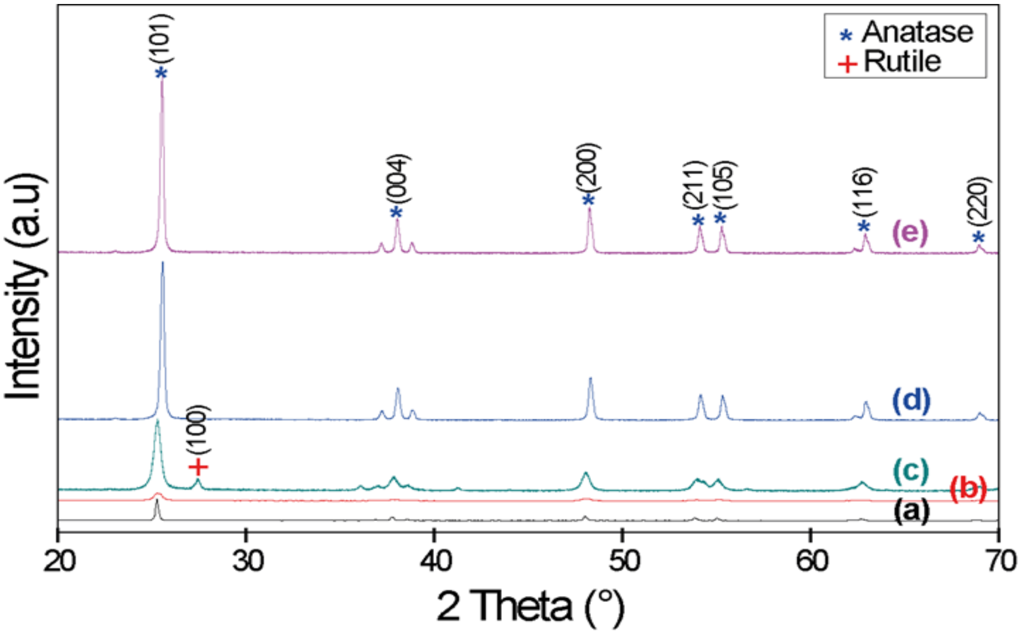

Fig. 1. X-ray powder diffraction spectra of: (a) $FeCl_3/TiO_2$= 0.1%, (b) $FeSO_4/TiO_2$= 0.2%, (d) $FeCl_3/TiO_2$= 0.2%, (c) TiO_2 pure, (e) $FeSO_4/TiO_2$= 0.1% calcined at 500°C.

Table 1. Sizes of pure and doped TiO_2 crystallite

Photocatalysts	Crystallite size (nm)
TiO_2	20.16
$FeCl_3/TiO_2$= 0.1%	43.01
$FeCl_3/TiO_2$= 0.2%	46.43
$FeSO_4/TiO_2$= 0.1%	48.34
$FeSO_4/TiO_2$= 0.2%	21.51

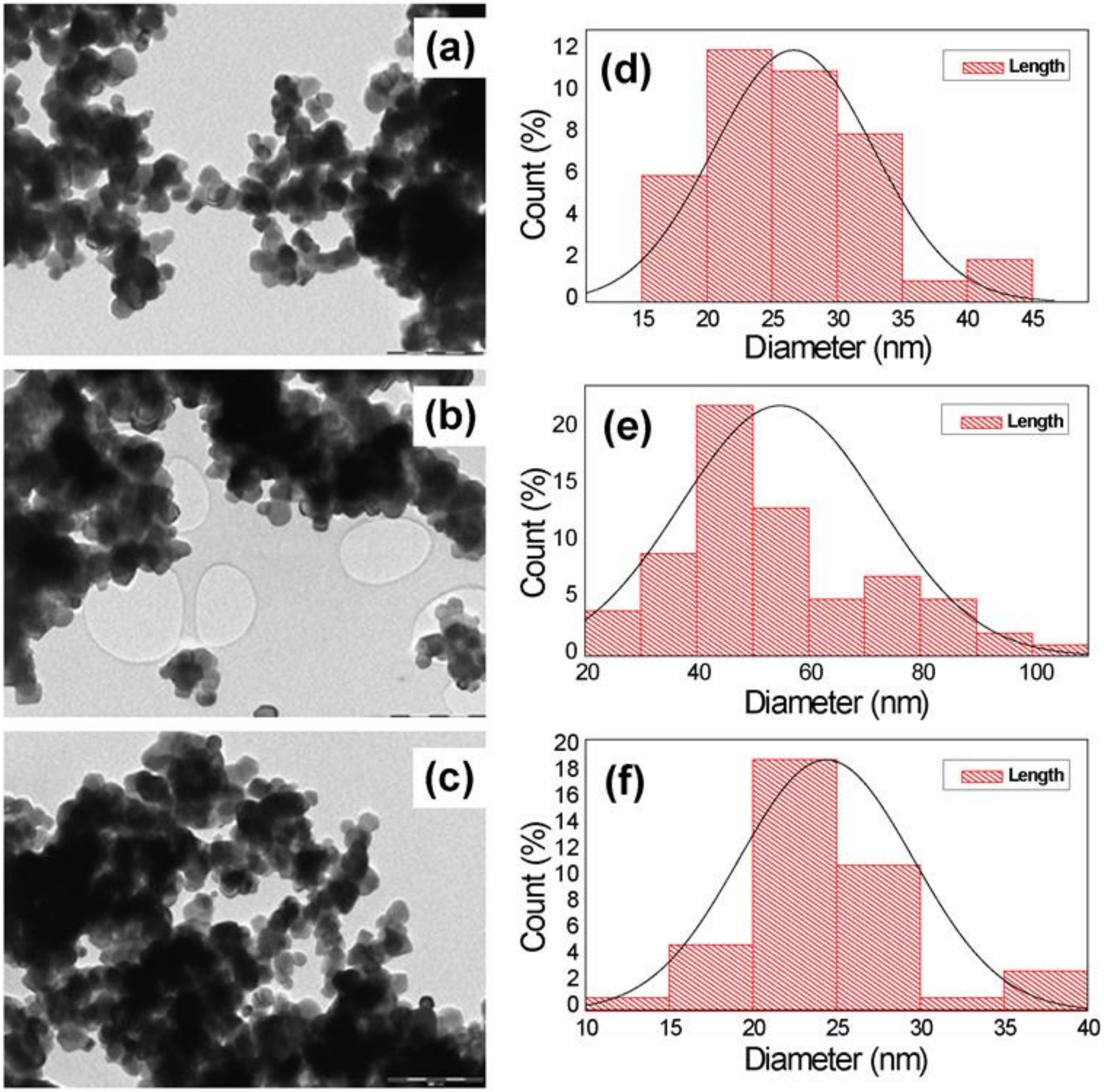

Fig. 2. TEM images of samples and the corresponding percentage count versus diameter: (a, d) TiO_2 pure, (b, e) $FeCl_3/TiO_2$= 0.2%, (c, f) $FeSO_4/TiO_2$= 0.2%.

3.4. Photodegradation of MO

To investigate the photocatalytic efficiency of prepared TiO_2 photocatalysts, we chose MO as a model pollutant compound because it is a common pollutant in industrial wastewater. **Fig. 5** shows the effect of added amounts of iron on the photocatalytic degradation of MO using synthesized TiO_2 powders. Compared to pure TiO_2, Fe-doped TiO_2 exhibits the highest photocatalytic efficiency. In fact, the presence of iron introduces a new energy level of transition metal ions between the valence conduction bands of TiO_2 [57], enhancing light absorption and improving the photocatalytic performance of TiO_2. Indeed, the absorption edge of Fe-doped TiO_2 is slightly shifted towards the onset wavelength. A plausible photocatalytic mechanism is proposed to explain the improved photocatalytic efficiency (**Fig. 6**). Comparison of MO degradation kinetics using TiO_2 and Fe-doped TiO_2 shows that pure TiO_2 is less active than 0.1% and 0.2% doped TiO_2 as they exhibit unmatched performance. The highest degradation efficiency was observed for 0.2% Fe-doped TiO_2, which was 4.2 times and 3.6 times higher than that of pure TiO_2, respectively.

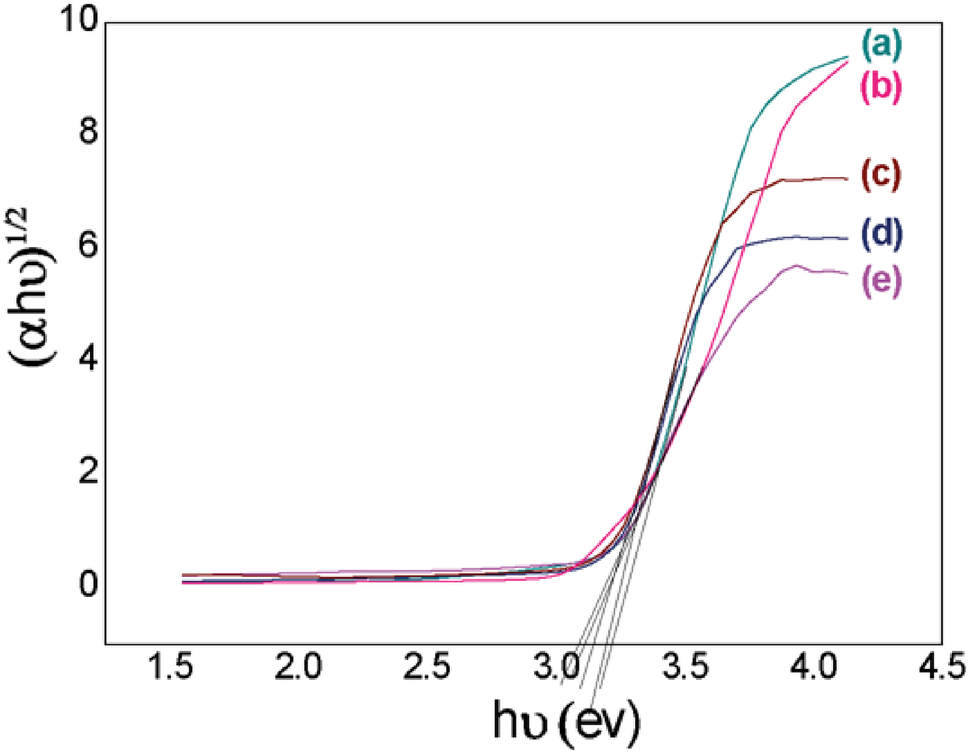

Fig. 3. Plots of $(\alpha h\upsilon)^{1/2}$ vs. photon energy (hυ) for (a) $FeSO_4/TiO_2$= 0.1%, (b) TiO_2 pure, (c) $FeCl_3/TiO_2$= 0.1%, (d) $FeCl_3/TiO_2$= 0.2%, (e) $FeSO_4/TiO_2$= 0.2%.

Table 2. Bandgap energies, absorption edges and potential positions of VB and CB of pure and doped TiO_2 calculated from the DRS spectra and using empirical formula data in the electronegativity scale of Mulliken.

Photocatalysts	Absorption edge (nm)	Band gap energy (eV)	E_{VB} (eV)	E_{CB} (eV)
TiO_2	380.37	3.26	2.434	-0.826
$FeCl_3/TiO_2$ =0.1%	387.50	3.20	2.404	-0.795
$FeCl_3/TiO_2$ =0.2%	388.71	3.19	2.399	-0.79
$FeSO_4/TiO_2$ =0.1%	386.29	3.21	2.409	-0.80
$FeSO_4/TiO_2$ =0.2%	391.54	3.17	2.389	-0.78

Examples of effective photocatalytic methods targeting different organic pollutants in different conditions are reported elsewhere [58, 59, 66-73]. **Table 4** shows examples of recently reported studies of the degradation effectiveness of some photocatalysts against wastewater treatment. For instance, synthesized Ag/TiO_2 photocatalysts with good Vis-L activity and good stability using sol-gel decomposition method were used to remove MO [60]. The wool-TiO_2 core-shell hybrid composite powder was prepared by ball milling technology to degrade MB [61]. In other studies, while the synergistic effect of TiO_2 with Ag and MoO_3 showed effective photocatalytic performance due to the extended absorption edge at longer wavelengths by reducing Eg [62], the increased photocatalytic efficiency of AO7 using metal-doped TiO_2 compared to undoped TiO_2 was found to be directly related to the production of large amounts of $^{\bullet}OH$ [63]. While activated carbon, carbon nanotubes, and biochar are frequently used, mixtures of adsorbents and TiO_2 have also revealed improved photocatalytic efficiency [64, 65]. Due to its synergic effect, adding an appropriate amount of biochar has been shown to improve the photocatalytic performance of TiO_2 [66]. In addition, mechanochemical methods were also used to produce TiO_2 with good photocatalytic activity [67]. Overall, most studies of dye photodegradation have focused on methylene blue, rhodamine B, and methyl orange [68, 69].

3.5. Suggested photocatalytic mechanism process using TiO_2

The mechanism of the photocatalytic degradation of organic pollutants, including dyes, using TiO_2 is usually initiated when an electron passes from the valence band

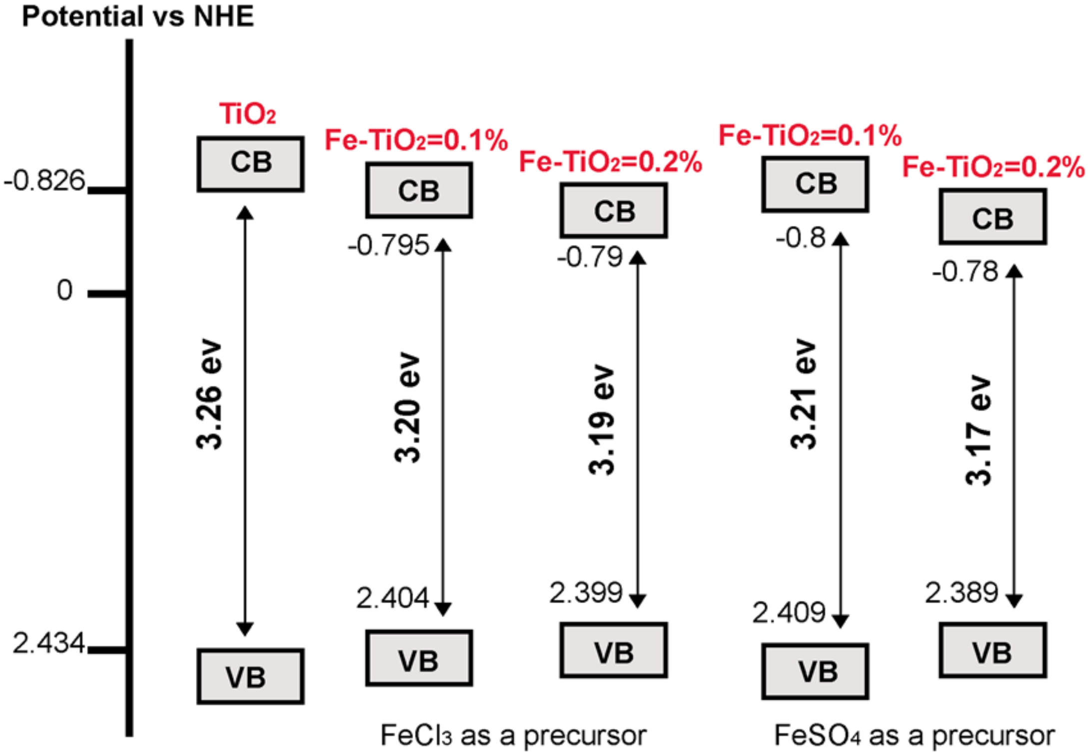

Fig. 4. Energy states diagrams of pure and Fe-TiO_2 samples.

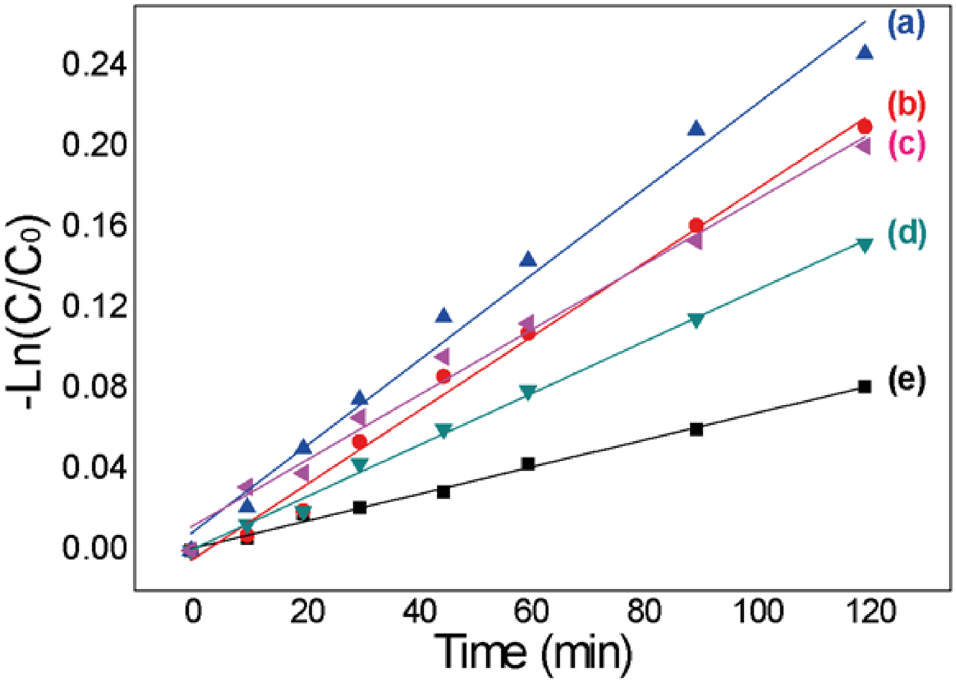

Fig. 5. Pseudo-first-order kinetics for MO dye (a) $FeCl_3/TiO_2$= 0.2%, (b) $FeSO_4/TiO_2$= 0.2%, (c) $FeCl_3/TiO_2$= 0.1%, (d) $FeSO_4/TiO_2$= 0.1%, (e) TiO_2 pure.

(BV) to the conduction band (BC), creating a hole (h^+) and an electron (e^-) [74], as represented in Eq (4):

$$TiO_2 \xrightarrow{hv} TiO_2 + h^+_{BV} + e^-_{BC} \qquad \text{Eq (4)}$$

On the one hand, the holes (h^+) oxidize the adsorbed water molecules or the hydroxyls anions (OH^-) and organic pollutants (R) on the surface of the photocatalyst to generate parallel hydroxyl $^{\bullet}OH$ and $R^{\bullet}$ radicals [26]. On the other hand, superoxide radicals ($O_2^{\bullet}$) could be formed by direct interaction of electrons and oxygen, or other electron acceptors [74, 75]. These

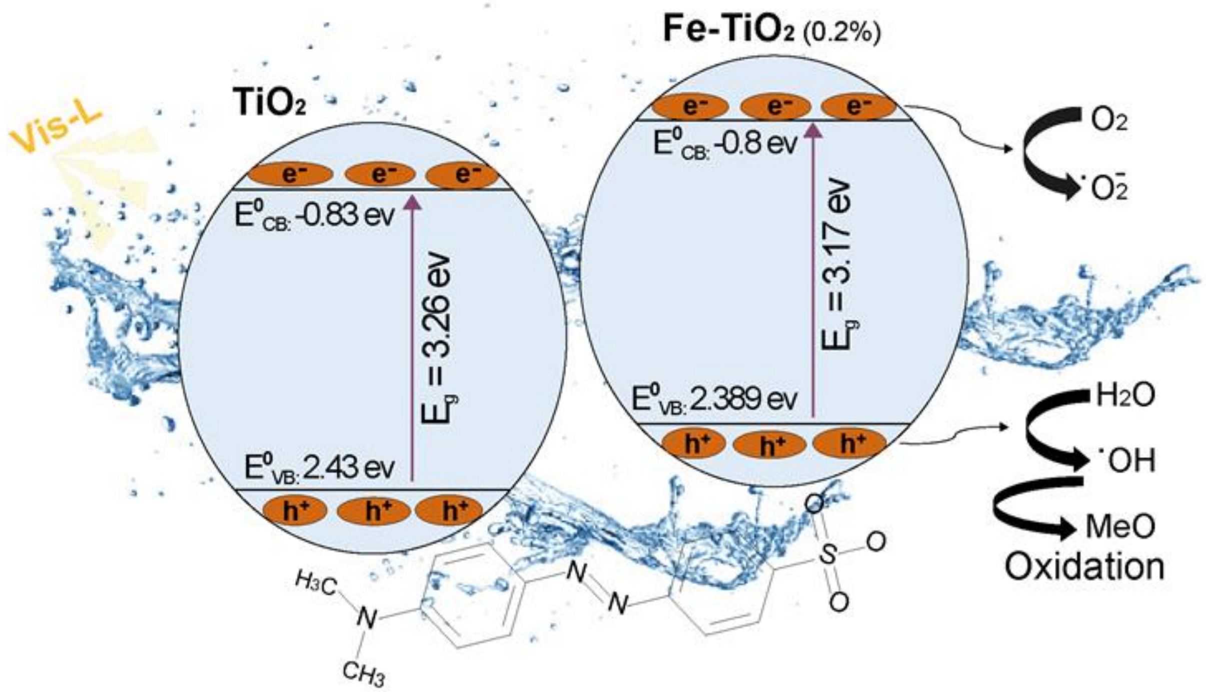

Fig. 6. Energy diagram for the charge carriers' transfer in TiO_2 and Fe-TiO_2.

processes are illustrated in the following Eqs (5, 6, 7, 8, 9):

$H_2O_{ads} + h^+ \rightarrow H^+ + {}^{\bullet}OH_{ads}$ Eq (5)

$OH^-_{ads} + h^+ \rightarrow {}^{\bullet}OH_{ads}$ Eq (6)

$R_{ads} + h^+ \rightarrow R^{\bullet}_{ads}$ Eq (7)

$O_2 + e^- \rightarrow O_2^{\bullet}$ Eq (8)

$TiO_2 + h^+_{BV} + e^-_{BC} \rightarrow TiO_2$ Eq (9)

The total degradation pathway of any R is represented in Eq (10). Indeed, the created hydroxyl radicals (${}^{\bullet}OH$) and oxygen during the photocatalytic processes are mainly responsible for the degradation of any R, including dyes.

$R + {}^{\bullet}OH \rightarrow CO_2 + H_2O$ Eq (10)

The potential effect of iron-doped cations on improving the photocatalytic efficiency of TiO_2 is due to the generation of Fe^{2+} cations, mainly linked to the process of transfer of electrons created from TiO_2 to Fe^{3+} [76]. Since Fe^{2+} cations are not stable, they transform into Fe^{3+} cations. Indeed, cations Fe^{2+} oxidize Fe^{3+} by moving electrons towards the absorbed O_2 to create superoxide anions (O_2^-). Moreover, Fe^{3+} cations could also act as an h^+ trap, due to the creation of an energy level for the redox couple (Fe^{3+}/Fe^{4+}) located over the energy level of TiO_2, causing reduction of cations Fe^{4+} to Fe^{3+} and transformation of hydroxyl groups (OH) into hydroxyl radicals (${}^{\bullet}OH$). These successive pathways are summarized in the following Eqs (11, 12, 13, 14):

$Fe^{3+} + 2\,e^- \rightarrow Fe^{2+}$ Eq (11)

$Fe^{2+} + O_{2(ads)} \rightarrow Fe^{3+}\ {}^{+}O_2^-$ Eq (12)

$Fe^{3+} + h^+ \rightarrow Fe^{4+}$ Eq (13)

$Fe^{4+} + OH^- \rightarrow Fe^{3+} + {}^{\bullet}OH$ Eq (14)

3.6. Kinetics of the MO photocatalytic process

Langmuir-Hinshelwood (L-H) equation is the most commonly used kinetic equation to describe the kinetic comportment of heterogeneous photocatalytic processes. In heterogeneous photocatalytic degradation experiments, Langmuir–Hinshelwood model was usefully applied to define the bonding linking the initial degradation rate and the initial concentration of an organic subtract, as given in Eqs (15, 16) [77]:

$r = -\,dC/dt = K_{\theta} = K\,(K_C/1+K_C)$ Eq (15)

$\ln\,(C/C_0) = -K\,K_t = -K_t'$ Eq (16)

Where r is the rate of reaction (mg L^{-1} min^{-1}), k the rate constant of the oxidation of the reactant/pollutant (mg L^{-1} min^{-1}), K is the rate constant of adsorption (L mg^{-1}) related to the energy of adsorption, C the concentration of dye solution (mg L^{-1}), C the concentration of the subjected reactant/pollutant (mg L^{-1}). The logarithmic form of the equation Eq (15) is given by Eq (16), which generally corresponds to an apparent first-order equation. Eq (16) is used to describe the kinetics of the heterogeneous photodegradation process when the catalyst organizes as one of the reactants in the solid phase and its concentration remains constant [78]. In this equation, C_0 and C_t represent the initial and final concentrations of the organic pollutant, t is the irradiation time, and k' represents the first-order apparent rate constant [79-81]. In fact, Eq (15) is zero-order at high concentrations ($C > 5\times10^{-3}$ mol L^{-1}), but at concentrations lower than 1×10^{-3} mol L^{-1}, the reaction follows an apparent first-order reaction [82]. **Table 3** and **Fig 5** show the values of the rate constant k and half-life $t_{1/2}$ of the powders and the photodegradation kinetics of MO using pure TiO_2 and Fe-doped TiO_2. The first-order rate constants of non-doped and Fe-doped TiO_2 declined in the following order $FeCl_3/TiO_2$ (0.2%) > $FeSO_4/TiO_2$ (0.2%) > $FeCl_3/TiO_2$ (0.1%) > $FeSO_4/TiO_2$ (0.1%) > TiO_2 (pure) reflecting progressive photocatalytic efficiency of each synthesized photocatalyst relative to the pure one (**Table 3**). The highest values of apparent rate constant and $t_{1/2}$ were found for $FeCl_3/TiO_2$ (0.2%) with corresponding values of $2.1x10^{-3}$ min^{-1} and 330 min, respectively. Our synthesized photocatalysts were successfully applied in the case of MO, and could be taken as generally applied nanomaterials to treat similar organic pollutants. This could lead to new standard methods in the field of photochemistry (particularly in heterogeneous phases) as well as in complex reaction and degradation experiments.

4. Conclusions

This study confirms that iron-doped TiO_2 improves the photocatalytic efficiency of MO photodegradation compared to pure TiO_2-P25. Fe-doped TiO_2 nanoparticles were prepared by the co-precipitation method and the XRD patterns did not show the presence of iron or iron oxide phases. We found that the particle size increases as the Fe/TiO_2 molar ratio increases and that the modified TiO_2 nanoparticles exhibited only an anatase phase. Optical results revealed a slight decrease in the bandgap energy, resulting in an increase in the wavelength of the absorption edge. The photocatalytic degradation process fits well with the Langmuir-Hinshelwood model.

Table 3. Kinetic parameters of doped and undoped TiO_2 under Vis-L.

Photocatalysts	K (min^{-1})	$t_{1/2}$ (min)
TiO_2	0.5 10^{-3}	1386
$FeCl_3/TiO_2$ =0.1%	1.6 10^{-3}	434
$FeCl_3/TiO_2$ =0.2%	2.1 10^{-3}	330
$FeSO_4/TiO_2$ =0.1%	1.3 10^{-3}	534
$FeSO_4/TiO_2$ =0.2%	1.8 10^{-3}	385

Table 4. Recent publications reporting the degradation effectiveness of some photocatalysts against wastewater treatment.

Catalysts	**Procedure**	**Description**	**Ref**
Ag/TiO_2/biochar composites	photo-deposition	MO degradation	[58]
TiO_2(Anatase)/WO_3/TiO_2(Rutile)	Sol-gel	MO degradation	[59]
TiO_2	Mechanochemical method	MO degradation	[66]
Nb_2O_5	Hydrothermal method	CR and MB degradation	[67]
$CuMn_2O_4$	Electrophoresis deposition (EPD) method	RhB and MO degradation	[68]
Co-$NiAl_2O_4$	Wet chemical synthesis route	MG degradation	[69]
CdS-ZnS	Deposition process	Rifampin degradation	[70]
CdS–Ag_3PO_4	Sol-gel	MB degradation	[71]
Mg-Al Oxide	Co-precipitation process	Phenol degradation	[72]

References

[1] S. Krishnan, H. Rawindran, C. M. Sinnathambi, J. W. Lim, Mater. Sci. Eng. 206 (2017) 012089.

[2] M. R. Hoffmann, S. T. Martin, W. Y. Choi, D.W. Bahnemann, Chem. Rev. 95 (1995) 69-96.

[3] A. Fujishima, T.N. Rao, D.A. Tryk, J. Photochem. Photobio. C 1 (2000) 1-21.

[4] G. Lofrano, G. Libralato, A. Casaburi, A. Siciliano, P. Iannece, M. Guida, L. Pucci, E. F. Dentice, M. Carotenuto, Sci. Total Envir. 624 (2018) 461-469.

[5]L. Gomathi Devi, R. Kavitha, RSC Adv. 4 (2014) 28265-28299.

[6]F. Huang, Y. Guo , S. Wang, S. Zhang, M. Cui, Sol. State Sci. 64 (2017) 62-68.

[7] A. Besharati-Seidani, Iran. J. Catal. 6(5) (2016) 447-454.

[8] Y. Ishibai, J. Sato, T. Nishikawa, S. Miyagishi, Appl. Catal. B 79 (2008) 117-121.

[9] J.M. Kwon, Y.H. Kim, B.K. Song, S.H. Yeom, B.S. Kim, J.B. Im, J. Hazard. Mater. 134 (2006) 230-236

[10] A.C. Mecha, M.S. Onyango, A. Ochieng, M.N.B. Momba, Sci. Total Environ. 601–602 (2017) 626–635.

[11] C. Noberi, F. Kaya, C. Kaya, Ceram. Int. 42 (2016) 17202–17209.

[12] M. Safari, M. Nikazar, M. Dadvar, J. Ind. Eng. Chem. 19 (2013) 1697–1702.

[13] O. Yadorao Bisen, R. Nandan, K. Kar Nanda, ACS Omega 5(51) (2020) 32852–32860.

[14] J.C.T. Lin, K. Sopajaree, T. Jitjanesuwan, M.C. Lu, (2018). Sep. Purif. Techno. 191(2018) 233-243.

[15] H. Khan, I.K. Swati, Ind. Eng. Chem. Res. 55 (2016) 6619–33.

[16] T. Ali, P. Tripath, A. Azam, W. Raza, S.A. Arham, A. Ateeq, M. Muneer, Res. Express 4 (2017) 015022

[17] S. Sood, A. Umar, S.K. Mehta, S.K. Kansal, J. Colloid. Interface Sci. 450 (2015) 213–23

[18] S. Yadav, G. Jaiswar, Review on Undoped/Doped TiO2 64(1) (2016) 103-16.

[19] M. Yeganeh, N. Shahtahmasebi, A. Kompany, M. Karimipour, F. Razavi, N.H.S. Nasralla, et al. Physica B: Condensed Matter. 511(2017) 89-98.

[20] M. Ghorbanpour, A. Feizi, J. Water Environ. Nanotechnol. 4(1) (2019) 60-66.

[21]H. Moradi, H. Eshaghi, S. R. Hosseini, K. Ghani, Ultrason .032 (2016) 314-319.

[22] L. Zeng, Z. Lu, M. Li, J. Yang, W. Song, D. Zeng, C. Xie, Appl. Catal. B (183) (2016) 308–316.

[23] M. E. Rockafellow, J. M. Haywood, T. Witte, R.S. Houk, W. S. Jenks, Langmuir 26 (24) (2010) 19052–19059.

[24]Z. Sheng, Y. Hu, J. Xue, X. Wang, W. Liao, Envir. Techn. 33 (2012) 2421-2428.

[25] M. Polat, A. M. Soylu, D. A. Erdogan, H. Erguven, E. I. Vovk, E. Ozensoy, Catal. Today (241) (2015) 25-32.

[26] J.M. Herrmann, F. in: Jansen, R.A. van Santen (Eds.), Catal. Sci. Series, London, Chapitre 9 (1) (1999) 171–194.

[27] S. Sehar, M. A.R. Hafiz, Y. Kamran, I. Mitsumasa,. J. Alloy.Comp. (737) (2018) 740-747.

[28] M. Humayun, F. Raziq, A. Khan, W. Luo, Green Chem. Lett. Rev. 11(2) (2018) 86-102.

[29] M. Madadi, M. Ghorbanpour, A. Feizi, Micro & Nano Lett. 13(11) (2018) 1590-1593.

[30] M. Madadi, M. Ghorbanpour, A. Feizi, Desalin. Water Treat. 145 (2019) 257-261.

[31] H. Yan-Xiao, Y. Chuan-Lu, W. Mei-Shan, M. Xiao-Guang, W. Li-Zhi, Sol. Energy Mater. Sol. Cells (132) (2015) 94–100.

[32] H. Zollinger, VCH Publishers, New York, 1991.

[33] C. Guillard, H. Lachheb, A. Houas, M. Ksibi, E. Elaloui, J.-H. Herrmann, J. Photochem. Photobiol. A: Chem. 158 (2003) 27–36.

[34] R. Cherrak, M. Hadjel, N. Benderdouche, Orient. J. Chem. 31 (2015) 1611-1620.

[35] L. G. Devi, K. M. Reddy, Appl. Surf. Sci. 256 (2010) 3116-3121.

[36] P. Singh, J. Sharma, Conference Proceedings 2006 (2018) 030029.

[37] M. M. Nassar, H. Y. Magdy, Chem. Eng. J. 66 (1997)223–226.

[38] B. Lellis, C. Z. Fávaro-Polonio, J. A. Pamphile, J. C. Polonio, 3 (2) (2019) 275-290.

[39] S. Ashraf, M. A. Rauf, S. Alhadrami, Dyes Pigments 69 (2006) 74–78.

[40]C. F. Patterson, Industrial Waste water Control, Academic Press, USA, 1991.

[41]U. Rott, R. Minke, Water Sci. Technol. 40 (1) (1999) 137–144.

[42]Z. Aksu, Process Biochem. 40 (2005) 997–1026.

[43] S. Ledakowicz, M. Solecka, R. Zylla, J. Biotechnol. 89 (2001) 175–184.

[44] M. Pera-Titus, V. Garcıa-Molina, M. A. Baos, J. Giménez, S. Esplugas, Appl. Catal. B: Environ. 47 (2004) 219–256.

[45] T. Oppenlander, Photochemical Purification of Water and Air, WILEY-VCH Verlag, 2003.

[46] M. Tekbas, H.C. Yatmaz, N. Bektas, Micropor. Mesopor. Mater. 115 (2008) 594–602.

[47] A. Aleboyeh, H. Aleboyeh, Y. Moussa, vol. 57, 2003, pp. 67–75.

[48] N. Riaz, F. Chong, B. K. Dutta, Z. B. Man, M. S. Khan, M. S. Third National Postgraduate Conference (NPC); IEEE: UniversityTeknologi PETRONAS (UTP), Tronoh, Malaysia, 1-5 (2011).

[49]H. Benelmadjat, B. Boudine, M. Halimi, M. Sebais, Opt. laser technol. 41(5) (2009) 630–633.

[50] Z. Wu, F. Dong, W. Zhao, S. Guo, (2008). J. Hazard. Mater. 157(1) (2008) 57-63.

[51] J. H. Tan, J. C. Sin, and S. M. Lam, IOP Conf. Series: Earth Env. Sci. 945 (2021) 12034.

[52] S. Mihai., D. L. Cursaru, D. Matei, et al. Sci Rep 9, (2019) 18798

[53]L. Jiang, S. Fernandez-Garcia, M. Tinoco, Z. Yan, Q Xue, G. Blanco, J. J. Calvino, A. B. Hungria, X. Chen, ACS Appl. Mater. Interfaces 9 (2017) 18595–18608.

[54]T. C. Paul, M.H. Babu, J. Podder, B. C. Dev, S. K. Sen, S. Islam, Phys. B Condens. Matter. 604 (2021) 412618.

[55] H. Irie, Y. Watanabe, K. Hashimoto, Chem. Lett. (32) (2003) 772-773.

[56] S.U.M. Khan, M. Al-Shahry, W. B. Ingler, Sci. (297) (2002) 2243-2245.

[57]I. Ellouzi, L. ELayazi, M. Hari, P. Schmitt-Kopplin, L. Laanab, H. Mountacer, S. El Hajjaji, Phys. Chem. News (75) (2015) 60-67.

[58] R. Shan, L. Lu, J. Gu, Y. Zhang, H. Yuan,Y. Chen, B. Luo, Mater. Sci. Semiconduct. Process.114 (2020) 105088.

[59] J. A. Pinedo-Escobar, J. Fan, E. Moctezuma, C. Gomez-Solís, C. J. Carrillo Martinez, E. Gracia-Espino. ACS Omega 6 (2021) 11840-11848.

[60] R. Saravanan, D. Manoj, J. Qin, M. Naushad, F. Gracia, A.F. Lee, M.M. Khan, M. A. Gracia-Pinilla, Process. Saf. Environ. 120 (2018)339–347.

[61] H. Gu, H. Zhang, X. Zhang, Y. Guo, L. Yang, H. Wu and N. Mao, Catalysts 11 (2021) 12-34.

[62] M. Hasan Khan Neon, M.S. Islam, Environ. Nanotechnol. Monit. Manag. 12 (2019) 100244.

[63] J. H. Shen, H. Y. Chuang, Z. W. Jiang, X. Z. Liu, J. L. Horng, Chemosph. 251 (2020) 126380.

[64] X. Xiong, I.K.M. Yu, L. Cao, D.C.W. Tsang, S. Zhang, Y.S. Ok, Bioresour. Technol. 246 (2017) 254–270.

[65] C. Qin, H. Wang, X. Yuan, T. Xiong, J. Zhang, J. Zhang, Chem. Eng. J. 382 (2020) 122977.

[66]L. Lu, R. Shan, Y. Shi, S. Wang, H. YuanChemosphere 222 (2019) 391–398.

[67]S. V. Kite, A. N. Kadam, D. J. Sathe, S. Patil, S. S. Mali, C. K. Hong, S.-W. Lee, K. M. Garadkar. ACS Omega 6 (2021) 17071-17085.

[68]S.D. Khairnar, M.R. Patil, V.S. Shrivastava, Iran. J. Catal. 8 (2018) 143–150.

[69]A. Sobhani- Eghbali-Arani, Nasab, M. S.M. Hosseinpour-Mashkani, F. Ahmadi, M. RahimiNasrabadi, V. Ameri, Iran. J. Catal. 10 (2018) 91–99.

[70]M. Arunkumar, A.S. Nesaraj, Iran. J. Catal. 10 (2020) 235–245.

[71] F. Soleimani, A. Nezamzadeh-Ejhieh, J. Mater. Res. Technol. 9 (2020) 16237–16251.

[72]S.A. Mirsalari, A. Nezamzadeh-Ejhieh, Mater. Sci. Semicond. Process. 122 (2021) 105455.

[73]M. Samandari, A.T. Manesh, S.A. Hosseini, S. Mansouri, Iran. J. Catal. 11 (2021) 175–180.

[74] A. N. Ejhieh, M. Khorsandi, J. Hazard. Mat. 176 (2010) 629–637

[75] J. Toth, J.coll. inter. Sci. 225 (2000) 378–383.

[76] A. R. Khan, R. Ataullah, A. Al−Haddad, J. Coll. Inter. Sci. 194 (1997) 154–165.

[77] MJ, Valero-Romero, JG, Santaclara, L. Oar-Arteta, L. van Koppen, DY. Osadchi, et al. Chem. Eng. J. 360 (2019) 75–88

[78]C. Martínez, M. I. Fern andez, J. A. Santaballa, J. Faria, Appl. Catal., B 107 (1-2) (2011) 110-118.

[79] R. Molinari, A. Caruso, L. Palmisano, J. Membr. Sci. Res. 3 (2010) 165-193

[80] J. Lin, L. Wang, C. Sun, 535–537 (2012) 2209–2213.

[81] G.V. Morales, E.L. Shan, R. Cornejo, E.M. Farfan Torres, Lat. Am. Appl. Res., 42 (2012)45–49.

[82] A. Nezamzadeh-Ejhieh, Z. Ghanbari-Mobarakehi, P, J. Ind. Eng. Chem., 21 (2015) 668–676.